Geophysical Journal International

Geophys. J. Int. (2023) **234,** 1012–1023
Advance Access publication 2023 March 17
GJI Geodynamics and Tectonics

https://doi.org/10.1093/gji/ggad118

The performance of differential point positioning using low-cost GNSS in comparison to DInSAR for monitoring coseismic displacement of the Provenzana–Pernicana fault system (Mt. Etna, 2018 December eruptive phase)

M.W. Wilkinson [1], A. Bonforte [2], R.R. Jones,[3] F.B. Wadsworth,[4] G.P. Roberts[5] and F. Guglielmino[2]

[1] *School of Engineering, Newcastle University, Newcastle Upon Tyne, UK. E-mail: max.wilkinson@ncl.ac.uk*
[2] *Istituto Nazionale di Geofisica e Vulcanologia, Sezione di Catania – Osservatorio Etneo. Piazza Roma,* 295125 *Catania, Italy*
[3] *Geospatial Research Ltd, Department of Earth Sciences, Durham University, UK*
[4] *Department of Earth Sciences, Durham University, UK*
[5] *Department of Earth and Planetary Sciences, Birkbeck College, Malet Street, London, WC1E 7HX, UK*

Received 2023 March 9; in original form 2022 September 30

SUMMARY

Mt. Etna is a perfect laboratory for testing new approaches and new technologies in a very active geodynamic environment. It offers, in fact, the opportunity for measuring active crustal deformation, related to volcanic activity as well as to seismic faulting on its flanks. In this work, a network of low-cost/low-power Global Navigation Satellite System stations has been installed and tested on Mt. Etna, across a very active fault, the Provenzana–Pernicana system, cutting its north-eastern flank. During the test period, a lateral eruption occurred (starting on 2018 December 24), with a forceful dyke intrusion that stressed all the flanks of the volcano, soliciting all the main faults dissecting the edifice. Also the Provenzana–Pernicana fault system, where this network was recording, was activated during the dyke intrusion, producing a significant seismic swarm. The low-cost/low-power network data analysis allowed the fault slip during the intrusion to be clearly traced in time and space at all the stations lying on the hangingwall mobile block of the fault. All the stations lying south of the fault trace showed an eastward displacement, in very good agreement with the usual kinematics of the fault and the temporal duration of the M 3.5 December 24 earthquake, related to the seaward dislocation of the eastern mobile flank of the volcano, promoted and accelerated by dyke emplacement on the upper part of the edifice.

Key words: Geodetic instrumentation; Satellite geodesy; Time-series analysis.

INTRODUCTION

The Provenzana–Pernicana fault system (PPFS) is one of the most active tectonic systems of Mt. Etna, cutting the NE flank of the volcano from the NE rift down to the coastline (Fig. 1a). The PPFS plays an important role in the dynamics of the mobile the eastern flank of the entire volcano. This fault system shows a complex kinematic behaviour, characterized by normal dip-slip and strike-slip mechanisms, which are not equally distributed along the fault (Acocella *et al.* 2003; Bonforte *et al.* 2011; Barreca *et al.* 2013; Cannata *et al.* 2021). Specifically, the eastern half of the PPFS system is dominated by almost aseismic, creeping strike-slip kinematics with left-lateral movement along E-W oriented fault planes, whereas the western half of the PPFS is seismic and dominated by normal deformation (Azzaro 2004; Bonforte *et al.* 2007a; Alparone *et al.* 2013; Barreca *et al.* 2013); this variation is observable particularly in ground deformation data. The seismicity related to the PPFS is characterized by the occurrence of isolated events or seismic swarms with substantial energy releases both in periods related to volcanic activity (e.g. before the 2002–2003 eruption; Bonforte *et al.* 2007b) as well as in non-eruptive periods (e.g. 2010 April seismic swarm; Guglielmino *et al.* 2011).

On 2018 December 24, Mt. Etna erupted volcanic ash from summit craters, accompanied by an important seismic swarm with hundreds of events mainly localized beneath the summit and on the upper SE flank, beginning from ∼08:30 UTC. Seismicity also affected the SW flank of the volcano and the NE sector, with significantly energetic events along the Pernicana fault. Initial eruption of clastogenic lava in the first few hours was fed by fountaining behaviour from the fissures, which then transitioned to effusive-vent fed lava

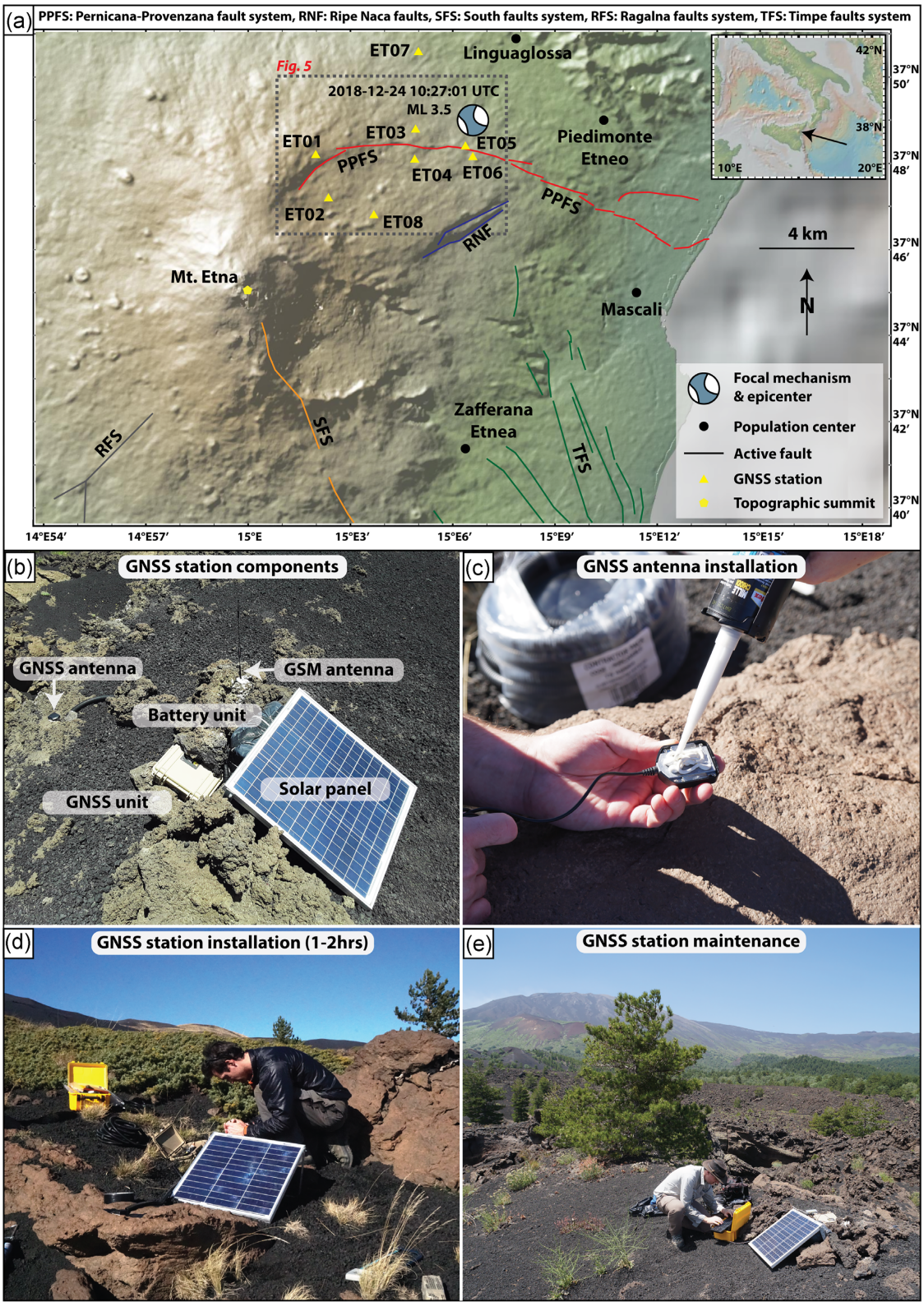

Figure 1. (a) Active faults, GNSS station locations and focal mechanism of the December 24, 10:27 UTC earthquake. Focal plane solution obtained from INGV, event no. 21 262 921. The Mercator projection has been used. Geographic co-ordinates are relative to the WGS84 datum. (b)–(e) GNSS station components, installation and maintenance.

flow until its cessation on December 27. Despite the relatively small size of the eruption, both in terms of duration and extension of lava field, the seismic swarm accompanying the eruptive phase was significant, in terms of number of events and their energy, with tens of events with $M > 3$. Based on these peculiarities, we infer the seismic swarm was generated by slip on many of the volcano-tectonic structures on the flanks of Etna, driven either by magma upwelling or widespread gravitational instability (Bonforte *et al.* 2019). Most of

Table 1. Low-cost GNSS station ID, geographic co-ordinates relative to the WGS84 datum and configuration.

Station ID	Latitude (decimal degrees)	Longitude (decimal degrees)	Ellipsoidal height (m)
ET01	37.80295	15.03317	2005
ET02	37.78611	15.03962	1884
ET03	37.81297	15.08200	1326
ET04	37.80119	15.08147	1442
ET05	37.80631	15.10609	1133
ET06	37.80243	15.10964	1110
ET07	37.84267	15.08303	926
ET08	37.77972	15.06167	1701

the earthquakes occurred below the upper SE flank, beneath the dry fracture formed during the 1989 eruption on an area that already showed seismic and ground deformation activity during previous recent eruptions (Bonforte *et al.* 2009, 2013). Furthermore, in the NE, the Pernicana fault was activated and, in the SW, the Ragalna fault (Neri *et al.* 2007) was also activated. Seismic swarms lasted for about 10 d, with a continuously decreasing energy, in terms of number of daily events and their magnitude (except for an $M_w = 4.9$ on the lower SE flank).

In this work, we analyse the displacement that occurred along the western and central parts of the PPFS, accompanying the eruptive phase of Mt. Etna, especially during the magma intrusion phase, characterized by high seismic energy release, fissure opening and fountaining eruptive activity at the new fissures and at the New South-East Crater (NSEC; Acocella *et al.* 2016). To characterize the dynamics accompanying the eruptive and seismic event, we present ground deformation collected by experimental low-cost Global Navigation Satellite System (GNSS) devices installed across the fault at different altitudes and collecting data at 1 Hz frequency. We also validate the results from our GNSS network with the 1-D Differential Interferometry Synthetic Aperture Radar (DInSAR) ground deformation maps obtained by processing C-band Sentinel-1A/B data on both ascending and descending orbits. In this way, we can obtain the detailed 3-D ground deformation pattern over the entire fault system. We combine the advantage of the high-frequency GPS system for investigating the evolution of the 3-D displacement of the fault in time and of the high spatial detail of DInSAR interferograms for defining the overall pattern of the cumulated ground deformation over the area.

METHODS

Low-cost GNSS network

From 2018 November 20, we started installing a network of eight low-cost GNSS stations along the PPFS and it was fully operational and actively recording from 2018 November 23 (named ET01–ET08; Table 1). The odd-numbered stations were positioned on the northern side of the PPFS (footwall), while even-numbered stations were positioned on the southern side (hangingwall). Stations were positioned to monitor displacement both within and between the northern and southern blocks separated by the PPFS (Fig. 1a). The network was set up as part of a GCRF[1]-funded proof-of-concept project to investigate the application of low-cost GNSS in the field of low-latency volcano monitoring. The stations consist of a low-cost single-frequency GNSS receiver, single board computer with a GSM modem and power management hardware housed in a Peli casing. The units are powered by a solar panel and lead-acid car battery. The point of observations for each GNSS unit is defined by a low-cost GNSS antenna which is attached to a flat and level bedrock surface using weatherproof adhesive (Fig. 1c). Single-frequency GNSS observations of pseudo-range, carrier phase, signal-to-noise ratio and doppler from the GPS, Galileo and GLONASS constellations are made by the GNSS receiver at 1 Hz intervals. The observations are output by the GNSS receiver and stored by the single board computer, which transmits the observations as hourly files to a data processing server over the GSM network using ftp. Initial positions of each low-cost GNSS station were calculated using Precise Point Positioning (PPP, Zumberge *et al.* 1997) via observations from 2018 November 23 to provide decimetre absolute accuracy as an input to subsequent differential processing. The GNSS observations from each station were processed in pairs by the server daily using differential positioning to reveal the position in east–west, north–south and up–down components of one GNSS station relative to another at 1 Hz temporal resolution. Hardware-based errors in the result of differential positioning are minimized as the same model of receiver and antenna are used for all stations in the network. Ionospheric and tropospheric delay are minimized in the differential positioning by minimizing baseline length between receivers. Short delay multipath is minimized through careful selection of station locations with minimal obstructions, while long-delay multipath and cycle-slips are identified and corrected for during data processing. The daily time-series data of 1 Hz positions were plotted as a graphical figure and uploaded to a web interface for immediate access by project scientists. The GNSS stations and data processing server combine to provide a complete automated low-cost GNSS monitoring system with low-latency visualization of time-series over the web.

DInSAR

The European Spatial Agency (ESA) Sentinel-1A/B (S1A/B) constellation allows the rapid generation of interferograms, thanks to a revisiting time of six days between two alternating passages of the two satellites over the same area in the same orbit. The Sentinel-1A and 1B C-band SAR (Synthetic Aperture Radar) data were exploited to image the ground deformation field accompanying the eruptive and seismic sequence occurring on Etna; we used the December 22–28 pair acquired in TopSAR (Terrain Observation with Progressive Scans SAR) Interferometric Wide mode on both ascending and descending orbit. Two 6-d interferograms (Fig. 2) were produced (Bonforte *et al.* 2019) by applying a two-pass DInSAR (Differential interferometry SAR) processing, using the GAMMA software and applying a multilook 5 × 1 (range and azimuth) to maintain the full ground resolution (11 × 13 m). For the topographic phase removal, a Shuttle Radar Topography Mission (SRTM) Version 4 digital

[1]Global Challenges Research Fund—https://www.ukri.org/our-work/collaborating-internationally/global-challenges-research-fund/

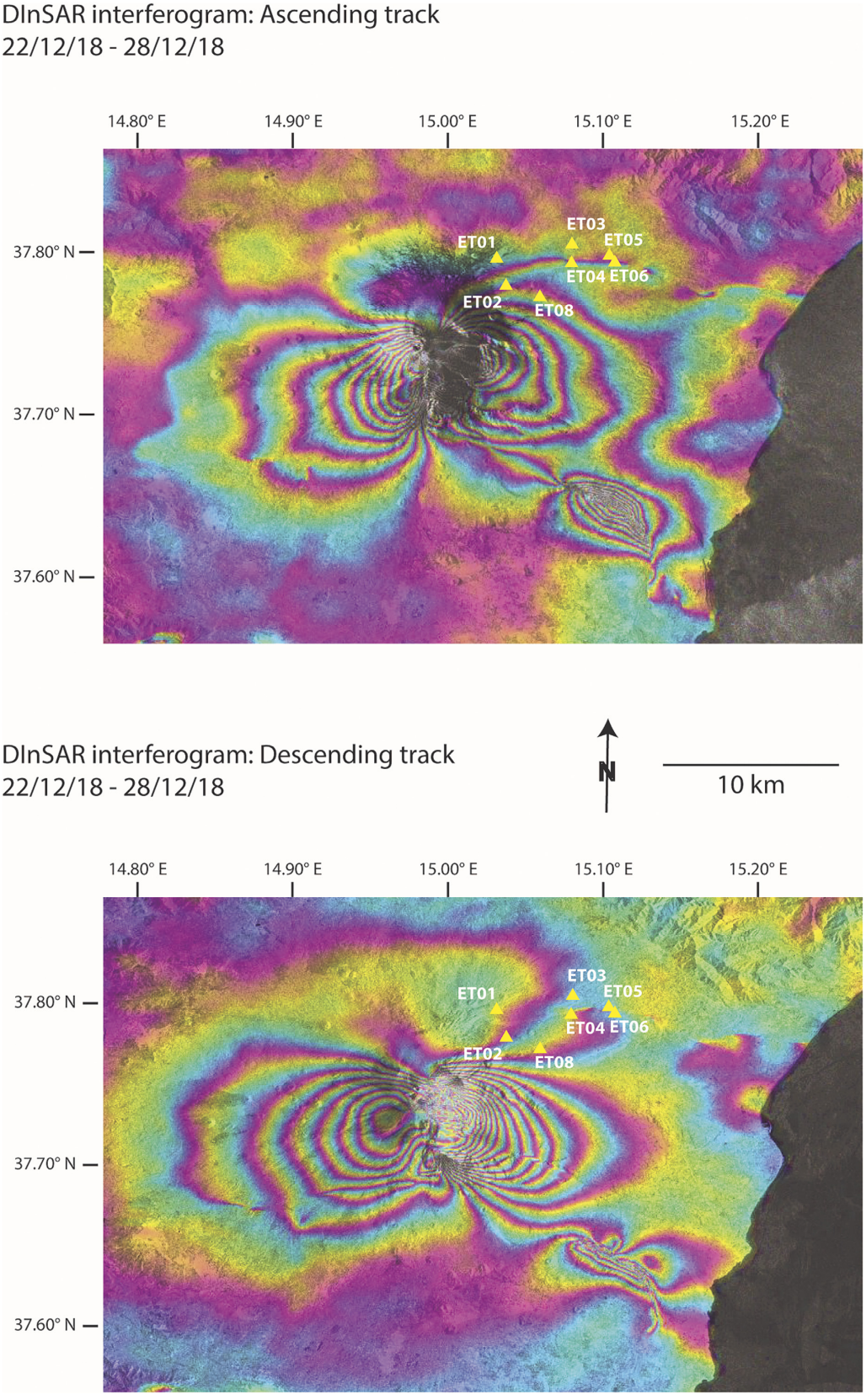

Figure 2. Ascending (top) and descending (bottom) DInSAR interferograms.

elevation model generated by SRTM with 3 arcsec resolution (about 90 m) was used (Jarvis *et al.* 2008).

RESULTS: DATA PROCESSING AND VALIDATION

GNSS time-series

We present time-series of relative position between pairs of low-cost GNSS stations within the network, derived using differential positioning, for the period between 2018 December 20 and 30 (Fig. 3 and Figs B1–B21, Supporting Information). Differential positioning was utilized using an initial position calculated using PPP. Due to the low-cost nature of the GNSS hardware (single-frequency GNSS receiver and antenna), differential positioning significantly improved the precision of the resultant positioning as opposed to that of PPP. Station ET07 did not record data during this period due to the antenna cable being chewed by some wildlife and so this station is excluded from the results. Stations ET01–ET06 and ET08 were used to create 21 baselines for this period (Table 2). The time-series for each baseline describe change in position of one GNSS station relative to another at as discrete lateral east–west, north–south and vertical up–down components (red, green and blue annotation, Fig. 3 and Figs B1–B21, Supporting Information). From an initial qualitative perspective, the time-series can be divided into two temporal periods separated by a transitional period within which we assume the variability of the position measurements are randomly distributed in time about a mean as follows: (1) a 'pre-period' 2018 December 20–23; (2) a transitional period of deviation from the pre-period mean 2018 December 24–27 and (3) a 'post-period' 2018 December 27−30, where deviation from the pre-period mean persists.

Quantitative statistical analysis of this time-series using the qualitatively defined periods described above was conducted by calculating the mean position and 3σ standard error of this mean in each component from the 1 Hz positional measurements for the four-day pre- and post-periods. The approach is to produce an average from many measurements and an estimate of precision. The means for each period are calculated using populations of $> 200\,000$ measurements, with 3σ standard error of the mean (SEM) per these populations reported at the micrometre-level, due to the large number of measurements within the population which are very close to the reported mean.

SEM is reported to describe the variance of the mean within a population where the noise may be significant, but the large population size over a long enough period may cause the noise to cancel out. The SEM provides an indication of the precision of the mean for each period, as opposed to the variance from the mean of any single measurement within a population. The SEM provides an indication of high precision in the calculated mean, in the cases where the noise is randomly distributed.

The relative-position axis of each component shown in the time-series (Fig. 3 and Figs B1–B20, Supporting Information) are normalized to the mean of the pre-period. Histograms for each component for the pre- and post-period populations are shown alongside the time-series to illustrate the distribution of the measurements about the mean. The change in the mean between the pre- and post-periods is then calculated for each component and reported in Table 2 for each baseline. A change in the mean between the pre- and post-periods is only considered significant following a qualitative assessment of each period to decide if the noise is randomly distributed about the mean, or if short-duration non-systematic noise or long-wavelength systemic noise exists within a period, which may produce a spurious deviation from the mean, as a function of period length or position with time.

The change in the means which pass and fail this test are shown in Table 2, as black and grey text, respectively. The east–west and north–south components are void of excessive long-wavelength systemic and short-duration non-systematic noise, suggesting the change in the means are robust and that precision is high. The vertical component is also mostly void of short-duration non-systemic noise. There is, however, significant long-wavelength systematic noise in all but the shortest baselines (ET01ET02, ET03ET04 and ET05ET06), which is typically attributed to spatial and temporal variation in the delay of the GNSS signals as they pass through the troposphere, from space, on their way to the GNSS antenna. The moisture content (so called wet component) of this tropospheric delay is particularly large and variable in space and time, and as such troublesome to model with any great accuracy (Hofmann-Wellenhof *et al.* 2012). The vertical component of any GNSS measurement is always of lower precision, in relation to the horizontal, due to the greater shielding effect of the earth in this direction.

The change in the means for all baselines in the east–west, north–south and vertical components were validated for network-wide consistency using a misclosure calculation of 35 unique baseline triplets (Fig. 4 and Table A1, Supporting Information). The misclosures are at the micrometre-level for all components, with errors in the east–west and north–south components typically an order of magnitude less than in the vertical, which as expected, signifies greater internal consistency of the measurements in these orientations. Network-wide minimal misclosures in relation to the magnitude of the delta means demonstrate a high degree of internal consistency, with confidence that non-systematic noise between different stations and baselines is insignificant. A component of highly systematic noise which would affect the measurements at each station in a consistent fashion cannot be discounted using this approach, hence we can conclude that the delta means are reported with high precision (relative accuracy between baselines is good, particularly in the horizontal components), but absolute accuracy is unknown. Hence, we can interpret the baseline delta means in terms of their relative differences (how they scale) across the network, but we cannot discount a network-wide systematic error which would affect the absolute accuracy of the delta means.

DInSAR interferograms

The ascending and descending interferograms produced for the same December 22–28 period allow imaging of the ground deformation pattern affecting the entire volcano from two opposite points of view (Fig. 2). From a general look at the scale of the volcano, the ascending view looks at the volcano from the WSW. Results show that the entire western side of Mt. Etna is approaching the satellite by ca. 8 fringes, meaning that it is moving upwards and/or westwards by around 20 cm on the uppermost part. Conversely, the eastern flank is moving away from the satellite by the same amount, revealing an eastward and/or downwards displacement. An opposite pattern affects the descending view, looking from the ESE, suggesting a dominant horizontal displacement of the edifice (the vertical deformation produces the same effect on both views), with a larger density of fringes on the uppermost eastern part of the volcano. Bonforte *et al.* (2019) have used these combined wide-scale

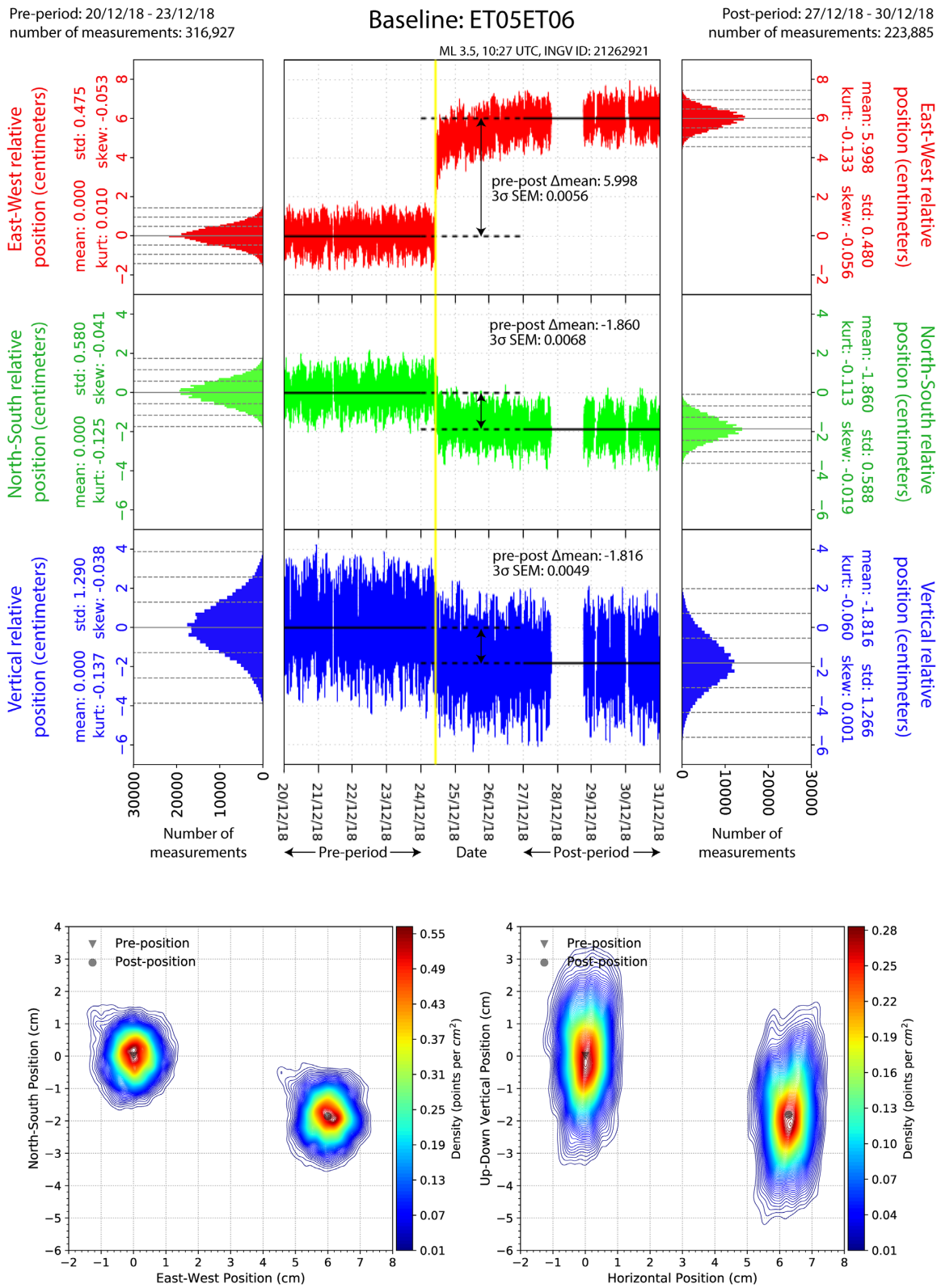

Figure 3. Time-series for baseline between GNSS stations ET05 and ET06 of relative position in east–west (red), north–south (green) and up–down (blue) components for the period 2018 December 20–31; 2018 December 24, 10:27 UTC earthquake on the Pernicana fault shown by the vertical yellow line. Histograms of the pre-period position are shown on the left of the time-series, while histograms of the post-period position are shown on the right of the time-series. In all cases, the mean for the pre- and post-period positions are shown as horizontal black lines up to the yellow line and extended beyond it to the right and left, respectively, as dashed lines. The difference between these pre- and post-period mean positions is the 'difference in means' referred to in the text and labelled here as Δmean along with the 3σ standard error associated with this determination. These same data for the distribution of positions about a mean are plotted in panels (b) and (c) as density maps.

Table 2. Baselines processed from the low-cost GNSS network, their attributes, intended purpose, delta-means, uncertainties and their inferred sense of displacement. Values in grey are those which failed the qualitative appraisal based on the presence of non-systematic noise.

Baseline	Length (m)	Azimuth (°)	ΔZ (m)	Monitoring purpose	Δmeans and 3σ SEM (cm) East–west	North–south	Vertical	Inferred sense of displacement
ET01ET02	1953	163	−121	Across fault deformation (PPFS)	3.199 (0.0041)	4.113 (0.0051)	−0.928 (0.0111)	Left-lateral
ET01ET04	4258	093	−563		3.611 (0.0056)	2.685 (0.0059)	0.611 (0.0182)	
ET01ET06	6735	090	−895		6.299 (0.0074)	1.398 (0.0087)	−0.322 (0.0087)	
ET01ET08	3599	136	−304		6.574 (0.0056)	5.239 (0.0062)	−0.439 (0.0145)	
ET03ET02	4778	231	558		2.670 (0.0057)	2.216 (0.0067)	−1.862 (0.0214)	
ET03ET04	1309	182	116		3.059 (0.0037)	0.764 (0.0051)	−0.252 (0.0115)	
ET03ET06	2701	116	−216		5.808 (0.0060)	−0.547 (0.0072)	−1.566 (0.0181)	
ET03ET08	4103	206	375		6.047 (0.0045)	3.335 (0.0060)	−1.411 (0.0172)	
ET05ET02	6269	249	751		2.867 (0.0068)	0.904 (0.0075)	−1.919 (0.0265)	
ET05ET04	2241	255	309		3.256 (0.0047)	−0.553 (0.0054)	−0.405 (0.0163)	
ET05ET06	533	144	−23		5.998 (0.0056)	−1.860 (0.0068)	−1.816 (0.0149)	
ET05ET08	4901	233	568		6.243 (0.0058)	2.033 (0.0068)	−1.489 (0.0228)	
ET01ET03	4442	075	−679	Intra-block deformation (north of PPFS)	0.522 (0.0058)	1.917 (0.0065)	0.999 (0.0206)	Anticlockwise rotation
ET01ET05	6433	087	−872		0.342 (0.0062)	3.251 (0.0072)	1.050 (0.0251)	
ET03ET05	2246	109	−193		−0.183 (0.0048)	1.326 (0.0054)	0.192 (0.0138)	
ET02ET04	4049	065	−442	Intra-block deformation (south of PPFS)	0.419 (0.0054)	−1.436 (0.0056)	1.530 (0.0185)	Clockwise rotation
ET02ET06	6428	074	−774		3.121 (0.0078)	−2.772 (0.0082)	0.606 (0.0284)	Clockwise rotation
ET02ET08	2068	110	−183		3.390 (0.0050)	1.123 (0.0056)	0.469 (0.0142)	Anticlockwise rotation
ET04ET06	2484	087	−332		2.751 (0.0057)	−1.305 (0.0066)	−1.223 (0.0188)	Clockwise rotation
ET04ET08	2953	216	259		2.981 (0.0042)	2.568 (0.0054)	−1.083 (0.0145)	Clockwise rotation
ET06ET08	4920	239	591		0.225 (0.0070)	3.877 (0.0081)	−0.049 (0.0263)	Anticlockwise rotation

patterns for modelling the magmatic intrusion; what we propose here is a detailed look into the local deformation imposed on the volcano-tectonic structures solicited by this wide displacement. Beside the outstanding feature related to the Fiandaca-Pennisi fault, showing a wide deformation on the SE side of Mt. Etna (Fig. 2) and related to the December 26 *M* 4.9 earthquake, we can observe also a local pattern of deformation on the NE flank, related to the Pernicana fault, where the GNSS network described in this paper is installed. Here, it is evident how the deformation fringes are shaped, driven and interrupted along the fault trace on both ascending and descending views. The deformation pattern depicted by the fringes reveals how the displacement of the eastern flank of the volcano, that appears to be induced by dyke intrusion, is confined by the Pernicana fault that decouples this mobile flank from the more stable northern one. There is about 1 fringe of displacement measured by DInSAR across the Pernicana fault, in the area of the GNSS network (Fig. 2). We can use the cumulative displacement observed by DInSAR from December 22 to 28 for a comparison and validation of measurements from the GNSS stations.

Comparison of GNSS time-series and DInSAR interferograms

A comparison between the GNSS- and DInSAR-derived measurements was conducted to investigate the validity of the low-cost GNSS approach to accurately capture small magnitude displacements. The two methods are treated independently. The change in the means between the pre- and post-periods (2018 December 20–23 and 27–30) for each GNSS baseline were resolved from the east–west, north–south and vertical up–down components into the line of sight (LOS) look direction on a point for point basis for the ascending and descending DInSAR tracks, Table 3, GNSS (pre-post

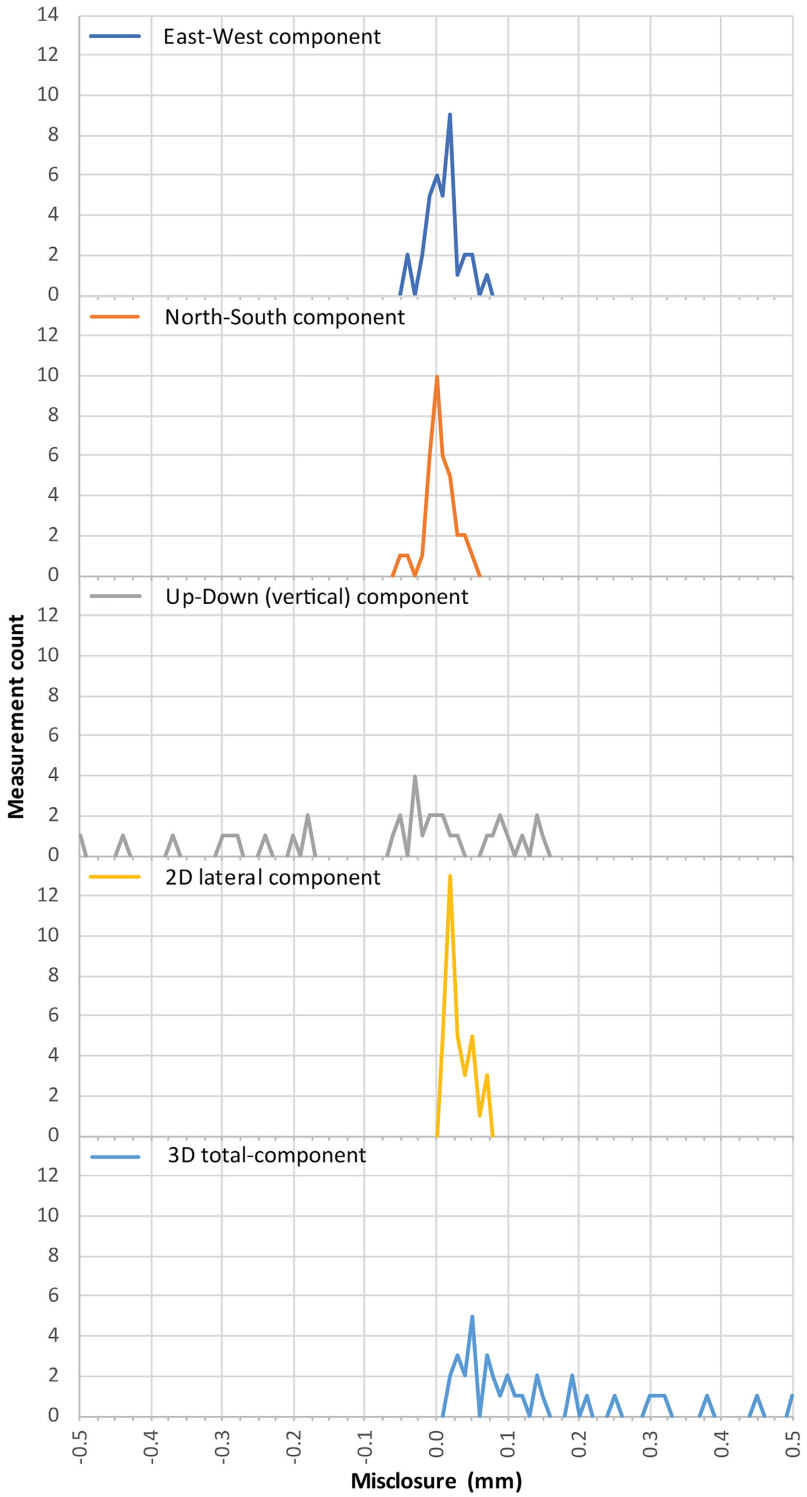

Figure 4. Validation of internal consistency of network of Δmeans using misclosure of baseline triplets (Table A1, Supporting Information), visualized as histograms for each component of displacement. Underlying data can be found in Supporting Information, Table A1.

delta means, resolved to DInSAR LOS in cm, ascending/descending columns). Corresponding measurements were derived from the DInSAR interferograms by differencing the LOS change at the locations of the GNSS stations at the ends of each baseline [Table 3, DInSAR (pre-post delta mean resolved in LOS, cm), ascending/descending columns]. These independent measurements are presented alongside each other in Fig. 5(a) as relative displacement per baseline. The differences between the GNSS-derived measurements relative to the DInSAR-derived measurements are in the range of −2.273 to 1.982 cm, with mean differences of −0.092 cm 0.263 SEM and −0.462 cm 0.230 SEM for the ascending and descending LOS, respectively [Table 3, difference comparison: GNSS relative to DInSAR (cm) and Fig. 5a, Difference between DInSAR and GNSS displacements].

Table 3. Per-baseline comparison of GNSS pre-post measurements to DInSAR LOS pre-post measurements.

GNSS baseline	DInSAR (pre-post delta LOS, cm)		GNSS (pre-post delta, resolved to InSAR LOS, cm)		Difference comparison: GNSS relative to DInSAR (cm)	
	Ascending	Descending	Ascending	Descending	Ascending	Descending
ET01ET02	− 3.373	0.689	− 3.445	0.397	− 0.072	− 0.292
ET01ET03	0.640	1.828	0.076	0.952	− 0.564	− 0.876
ET01ET04	− 2.461	2.779	− 2.449	2.062	0.011	− 0.718
ET01ET05	1.531	2.342	0.077	0.789	− 1.454	− 1.553
ET01ET06	− 2.961	4.958	− 4.856	2.685	− 1.895	− 2.273
ET01ET08	− 5.607	3.274	− 5.501	2.377	0.105	− 0.896
ET02ET04	0.912	2.091	0.981	1.659	0.069	− 0.431
ET02ET06	0.412	4.270	− 1.391	2.302	− 1.802	− 1.968
ET02ET08	− 2.234	2.585	− 2.096	1.969	0.138	− 0.616
ET03ET02	− 4.013	− 1.139	− 3.456	− 0.502	0.557	0.637
ET03ET04	− 3.101	0.952	− 2.385	1.214	0.716	0.262
ET03ET05	0.891	0.515	0.096	− 0.041	− 0.794	− 0.556
ET03ET06	− 3.601	3.131	− 5.074	1.539	− 1.473	− 1.592
ET03ET08	− 6.247	1.446	− 5.527	1.445	0.719	− 0.001
ET04ET06	− 0.500	2.179	− 2.603	0.404	− 2.103	− 1.775
ET04ET08	− 3.146	0.494	− 3.104	0.295	0.042	− 0.200
ET05ET02	− 4.903	− 1.653	− 3.462	− 0.338	1.441	1.315
ET05ET04	− 3.991	0.437	− 2.451	1.294	1.540	0.857
ET05ET06	− 4.492	2.616	− 5.199	1.532	− 0.707	− 1.085
ET05ET08	− 7.137	0.932	− 5.532	1.590	1.605	0.658
ET06ET08	− 2.646	− 1.685	− 0.663	− 0.276	1.982	1.408
				Mean difference (cm)	− 0.092	− 0.462
				SEM (cm)	0.263	0.230

Total least squares regression was used to calculate the best estimation of the linear relationship between the two independent measurements as a means to validate the GNSS-derived measurements against the DInSAR-derived measurements (Fig. 4b, black dashed line, straight line equation $y = mx + c$).The DInSAR measurements are given as the model (x) values and the GNSS measurements as the dependant variable (y). Cross plots of the independently derived relative displacements for the two methods in the ascending and descending look directions are shown in Fig. 5(b). They represent strong positive correlations with goodness of independent agreement (R^2) values of 0.766 and 0.754 for the ascending and descending look directions. The regressions pass close to the origin in both cases. The data set in the ascending look direction has a gradient closer to the expected parity value of 1 (0.810) than that of the descending (0.494). The better fit of the ascending data set was expected, since the geometry of the deformation processes on this sector of the volcano produces a better signal-to-noise ratio for the eastwards looking passes, as well described in Bonforte *et al.* (2011). For completeness, regression with a fixed gradient of 1 was also conducted and is shown by the blue and red dash lines in Fig. 5(b) for the respective ascending and descending data sets. The observed correlation is statistically significant for both ascending and descending data sets, with p-values of 2.061E-07 and 3.401E-07 respectively. Scatter perpendicular to the regression line is up to 1.6 and 1.0 cm for the ascending and descending LOS with most data points within 0.6 cm. Mean differences between the two data sets on a per-station basis were calculated by averaging the differences for all baselines which reference a particular station. For instance, the mean for station ET01 is calculated using the results from baselines ET01ET02, ET01ET03, ET01ET04, ET01ET05, ET01ET06 and ET01ET08. The per-station means range from 0.630 to 1.682 cm. There is typically little difference between the results for the ascending and descending LOS. Stations ET05 and ET06 have the highest mean differences whilst the remaining stations are consistently of a lower mean difference (Fig. 5c). The mean of the mean differences for all stations are 0.942 and 0.951 cm for the ascending and descending LOS with variances of 0.140 and 0.136 cm.

DISCUSSION

Appraisal of the GNSS baseline time-series results using the combined quantitative–qualitative approach is considered in the context of the historical tectono-volcanic activity on Etna and that during the period 2018 December 20–31. The derived difference in means in east–west and north–south components are considered in the context of the PPFS (Fig. 1a), a consistent left-lateral tectonic feature in past geological and geophysical studies in this region of Etna (Tibaldi & Groppelli 2002; Acocella & Neri 2005; Bonforte *et al.* 2007a, 2011; Alparone *et al.* 2011; Barreca *et al.* 2013). These difference in means show strong spatial correlation with the PPFS, its left-lateral long-term geological displacement and the left-lateral focal mechanism of the M 3.5 earthquake. Displacement relative to the northern block (ET03) and the southern block (ET08) in all cases describe lateral position change consistent with left-lateral motion, in correlation with the sense of longer-term geological displacement across the PPFS (Fig. 6). The resolved orientations of the lateral motions also vary in accordance with the change in strike of the PPFS along its length, becoming less north–south and more east–west from west to east along strike. Displacements of stations in the northern block of the PPFS, relative to station ET03 (Fig. 6, light blue vectors) also describe left-lateral motion, albeit of reduced magnitude compared to stations in the southern block, consistent with segmentation and probably a clockwise rotation of this northern block by left-lateral subsidiary faults and shear zones. Displacement of stations within the southern block, relative to station ET08 (Fig. 6, green vectors) display position change consistent with both left- and right-lateral motion, highlighting the complex nature of the southern side of

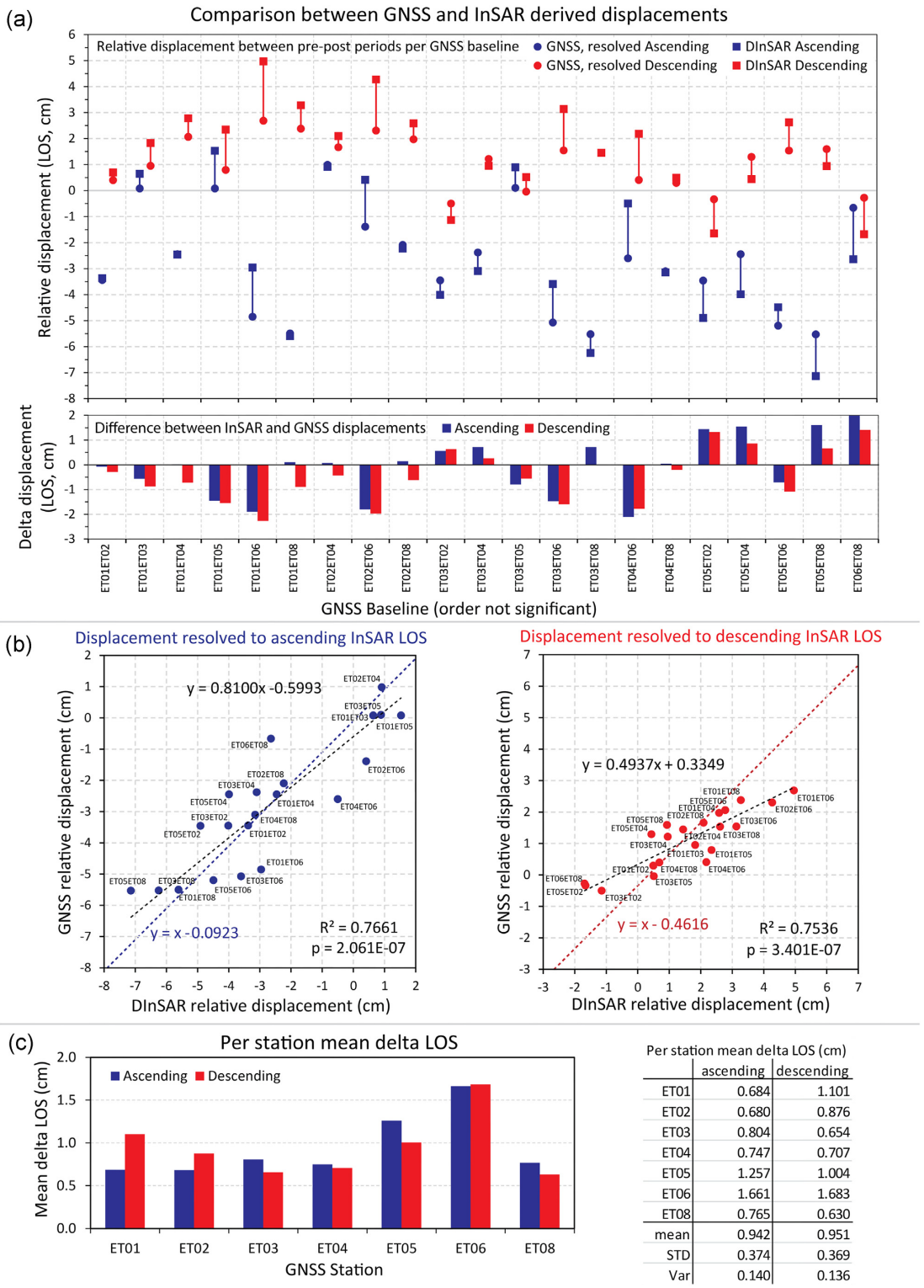

Per station mean delta LOS (cm)

	ascending	descending
ET01	0.684	1.101
ET02	0.680	0.876
ET03	0.804	0.654
ET04	0.747	0.707
ET05	1.257	1.004
ET06	1.661	1.683
ET08	0.765	0.630
mean	0.942	0.951
STD	0.374	0.369
Var	0.140	0.136

Figure 5. Comparison between GNSS and DInSAR derived displacements. (a) Relative displacement for each baseline between the pre- and post-periods resolved in the ascending and descending look directions; difference between the DInSAR and GNSS derived displacements. (b) Scatter plots of DInSAR relative displacement versus GNSS relative displacements in the ascending and descending look directions. The regression presented as the black dashed line is calculated using total least squares. (c) Per station mean delta for ascending and descending tracks calculated using the difference data in (a) for each baseline containing the station.

the PPFS where a simple tectonic block model cannot fully explain the sense of motion recorded. Instead, it is likely that this block here is segmented in the form of subsidiary faults with a range of orientations; in fact, our data show a complex distribution of the deformation suggesting a sort of segmentation of the southern block of the fault by some conjugate faults, similarly to those shown in fig. 9 of Bonforte *et al.* (2007a). The contrast in displacement style, magnitude and internal consistency of displacements on the

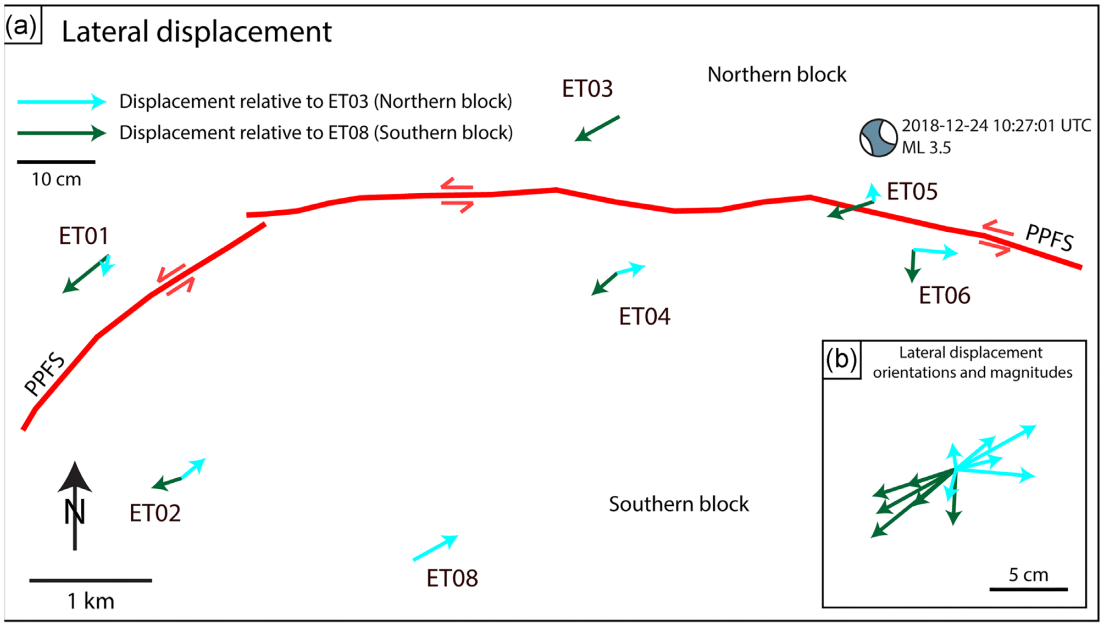

Figure 6. (a) Inset from Fig. 1(a). Spatial distribution of inferred lateral displacements relative to the northern block (station ET03) and southern block (ET08). (b) Distribution of displacement orientations and magnitudes for, colours as in (a). Focal plane solution obtained from INGV, event no. 21 262 921.

northern and southern sides of the PPFS and those constrained to the northern and southern blocks is clear and unequivocal in this data set. The inferred lateral displacement vectors are clustered in their orientation (Fig. 6b), relative displacements of stations that cross the PPFS display orientations in the east–north–east west–south–west domain, while relative displacements of stations within the northern block are tightly clustered in the north–south domain and the relative displacements of stations within the southern block are more dispersed in the north–south domain.

The detailed temporal record of motion described by the time-series for each baseline is complex and detailed analysis will the focus of a future work, however it is clear in almost all baselines that these motions initially occurred during the first half of the 2018 December 24 which led to a finite change in position of one GNSS relative to another. The baselines show a range of different temporal responses, from focused rapid motion (ET05ET06) to a more distributed response (ET01ET04 and ET01ET06, Supporting Information Figs B3 and B5). A detailed appraisal of the temporal response is ongoing; however, it is worth brief consideration here. The 2018 December 24 was typified by intense tectonic and volcanic activity, with an increased rate of eruption of ash at the summit craters followed by a strong seismic swarm, with tens of events $M > 3$. Of these events, only one located on the PPFS within our GNSS network with M_L 3.5 and a source time of 10:27 UTC (INGV ID: 21 262 921). The source time is illustrated on each time-series figure as a yellow vertical line, the epicentre and focal mechanism is shown on Figs 1(a) and 5(a). The proximity of this earthquake to our network and its source time in relation to the shift in position seen in all baselines along with the spatial correlation of across fault baseline delta means between the pre- and post-periods is sufficient to consider this seismic event as the source of the finite position change. We thus interpret this as a direct measurement of displacement along the PPFS as fault slip in response to this earthquake, but with variable duration of slip.

The significant outcome from this work is therefore the demonstration of the use of low-cost GNSS for the monitoring of subtle surface displacement at the millimetric level. Such measurements act as an important independent validation of remote sensed measurements such as InSAR. The data sets here demonstrate the low-cost approach has sufficient sensitivity and temporal resolution to be used as a tool to monitor position change within a network of stations and to use these to infer subtle fault displacements related to specific seismic events.

CONCLUSIONS

We acquired 1 Hz data from a self-installed low-cost GNSS network of seven stations in the near-field during the 2018 December eruptive-phase and seismic crisis of Etna. Using this data, we show that low-cost GNSS networks are a suitable tool for the monitoring of local volcano-tectonic deformation and fault slip, with submillimetric internal consistency by post-processing. Further, we compare the relative displacements between pairs of low-cost GNSS stations within the network to those derived from DInSAR over the same period to validate the relative accuracy at a subcentimetric level, with standard deviations of up to 1.2 cm. Such low-cost GNSS networks are a valuable tool for monitoring the temporal evolution of both distributed deformation and discrete deformation focused on active faults. When combined with the well-established DInSAR approach to monitor surface deformation at the millimetric level, low-cost GNSS provides a means of populating the temporal domain with measurement rates of 1 Hz, where DInSAR can only currently provide repeat times of 6 + days. The high measurement frequency of low-cost GNSS also holds promise for the delivery of post-processed data describing volcano-tectonic deformation. This work acts as validation of the accuracy of the low-cost GNSS approach in this setting and forms the basis for future exploration of the potential of low-cost GNSS as a low-latency monitoring tool for active volcanoes with sparse instrumentation, such as in the developing world.

ACKNOWLEDGMENTS

This research was funded in part by the Global Challenges Research Fund in relation to its applicability to the developing world. The authors want to thank the periodic survey group of INGV-Osservatorio Etneo, Jenny Schauroth and Sébastien Gilment for their support to the fieldwork during installation and for the maintenance of the stations.

DATA AVAILABILITY

The data underlying this paper will be shared on reasonable request to the corresponding author.

REFERENCES

Acocella, V., Behncke, B., Neri, M. & D'Amico, S., 2003. Link between major flank slip and 2002–2003 eruption at Mt. Etna (Italy), *Geophys. Res. Lett.,* **30**(24), 2286. doi:10.1029/2003GL018642

Acocella, V. & Neri, M., 2005. Structural features of an active strike–slip fault on the sliding flank of Mt. Etna (Italy), *J. Struct. Geol.,* **27,** 343–355.

Acocella, V, Neri, M, Behncke, B, Bonforte, A, Del Negro, C & Ganci, G, 2016. Why does a mature volcano need new vents? The case of the new southeast crater at Etna, *Front. Earth Sci.,* **4,** 67. doi: 10.3389/feart.2016.00067

Alparone, S., Barberi, G., Bonforte, A., Maiolino, V. & Ursino, A., 2011. Evidence of multiple strain fields beneath the eastern flank of Mt. Etna volcano (Sicily, Italy) deduced from seismic and geodetic data during 2003–2004, *Bull. Volcanol.,* **73,** 869–885.

Alparone, S, Bonaccorso, A, Bonforte, A & Currenti, G, 2013. Long-term stress-strain analysis of volcano flank instability: the eastern sector of Etna from 1980 to 2012, *J. geophys. Res.,* **118,** 5098–5108

Azzaro, R., 2004. Seismicity and active tectonic in the Etna region: constrain for seismotectonic model, in: Bonaccorso, A., Calvari, S., Coltelli, M., Del Negro, C. & Falsaperla, S.(Eds.), *Mt. Etna Volcano Laboratory. Am. Geoph. Union (Geophysical monograph series)*. American Geophysical Union, vol. **143,** pp. 205–220.

Barreca, G, Bonforte, A & Neri, M(2013). A pilot GIS database of active faults of Mt. Etna (Sicily): a tool for integrated hazard evaluation, *J. Volc. Geotherm. Res.,* **251,** 170–186.

Bonforte, A., Branca, S. & Palano, M., 2007a. Geometric and kinematic variations along the active Pernicana fault: implication for the dynamics of Mount Etna NE flank (Italy), *J. Volc. Geotherm. Res.,* **160,** 210–222

Bonforte, A., Gambino, S., Guglielmino, F., Obrizzo, F., Palano, M. & Puglisi, G., 2007b. Ground deformation modeling of flank dynamics prior to the 2002 eruption of Mt. Etna, *Bull. Volcanol.,* **69,** 757–768

Bonforte, A., Gambino, S. & Neri, M., 2009. Intrusion of eccentric dikes: the case of the 2001 eruption and its role in the dynamics of Mt. Etna volcano, *Tectonophys*., **471,** 78–86

Bonforte, A., Guglielmino, F., Coltelli, M., Ferretti, A. & Puglisi, G., 2011. Structural assessment of Mount Etna volcano from Permanent Scatterers analysis, *Geochem. Geophys. Geosyst.,* **12,** Q02002, doi:10.1029/2010GC003213.

Bonforte, A, Guglielmino, F & Puglisi, G, 2013. Interaction between magma intrusion and flank dynamics at Mt. Etna in 2008, imaged by integrated dense GPS and DInSAR data, *Geochem. Geophys. Geosyst.,* **14,** 2818–2835.

Bonforte, A., Guglielmino, F. & Puglisi, G., 2019. Large dyke intrusion and small eruption: the December 24, 2018 Mt. Etna eruption imaged by Sentinel-1 data, *Terra Nova,* **31,** 405–412

Cannata, A., *et al.* 2021. Repeating earthquakes and ground deformation reveal the structure and triggering mechanisms of the Pernicana fault, Mt. Etna, *Comm Earth and Environ.,* **116,** doi:10.1038/s43247- 021-00188-6.

Guglielmino, F., Bignami, C., Bonforte, A., Briole, P., Obrizzo, F., Puglisi, G., Stramondo, S. & Wegmuller, U., 2011. Analysis of satellite and in situ ground deformation data integrated by the SISTEM approach: the April 3, 2010 earthquake along the Pernicana fault (Mt. Etna - Italy) case study, *Earth Planet. Sci. Lett.,* **312,** 327–336.

Hofmann-Wellenhof, B., Lichtenegger, H. & Collins, J., 2012. *Global Positioning System: Theory and Practice*. Springer Science & Business Media.

Jarvis, A., Reuter, H., Nelson, A. & Guevara, E., 2008. *Hole-filled seamless SRTM data V4. Tech. rep., International Centre for Tropical Agriculture (CIAT)*. Cali, Columbia.

Neri, M., Guglielmino, F. & Rust, D., 2007. Flank instability on Mount Etna: radon, radar interferometry and geodetic data from the southwestern boundary of the unstable sector, *J. geophys. Res.,* **112,** doi:10.1029/2006JB004756.

Tibaldi, A. & Groppelli, G., 2002. Volcano-tectonic activity along tructures of the unstable NE flank of Mt Etna (Italy) and their possible origin, *J. Volc. Geotherm. Res.,* **115,** 277–302.

Zumberge, J.F., Heflin, M.B., Jefferson, D.C., Watkins, M.M. & Webb, F.H., 1997. Precise point positioning for the efficient and robust analysis of GPS data from large networks, *J. geophys. Res.,* **102**(B3), 5005–5017.

SUPPORTING INFORMATION

Supplementary data are available at *GJI* online.

Supplementary material.docx

Please note: Oxford University Press is not responsible for the content or functionality of any supporting materials supplied by the authors. Any queries (other than missing material) should be directed to the corresponding author for the paper.